Research Article Vol. 3, No. 2 / 25 April 2025 / Optica Quantum 211

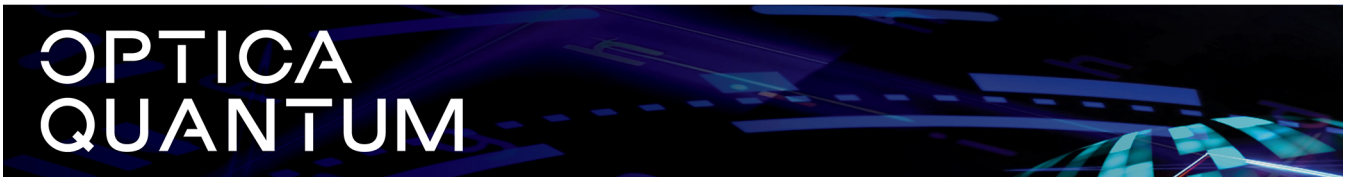

Heralded telecom single photons from a visible–telecom pair source on a hybrid PPKTP–PIC platform

Vijay S. S. Sundaram,[1,*] Evan Manfreda-Schulz,[1] Todd Hawthorne,[2] Tony Roberts,[2] Thomas Palone,[1] Venkatesh Deenadayalan,[1] Mario Ciminelli,[1] Phil Battle,[2] Gerald Leake,[3] Daniel Coleman,[3] Michael L. Fanto,[1,4] Nick Vamivakas,[5] Gregory A. Howland,[1] and Stefan F. Preble[1]

[1]Microsystems Engineering, Rochester Institute of Technology, Rochester, New York 14623, USA
[2]AdvR Inc, 2310 University Way, Bldg. 1-1, Bozeman, Montana 59715, USA
[3]State University of New York Polytechnic Institute, Albany, New York 12203, USA
[4]Air Force Research Laboratory, Rome, New York 13441, USA
[5]Institute of Optics, University of Rochester, New York 14623, USA
*vs8972@rit.edu

Received 21 November 2024; revised 31 March 2025; accepted 2 April 2025; published 22 April 2025

We present a heralded photon-pair source using periodically poled potassium titanyl phosphate (PPKTP) waveguides coupled with photonic integrated circuits (PICs). The PPKTP generates correlated visible–telecom photon pairs, processed by the dual-band silicon and silicon nitride PIC. Heralding at visible wavelengths removes the need for large superconducting nanowire single-photon detectors (SNSPDs). Silicon Mach–Zehnder interferometers (MZIs) on the PIC modulate the telecom single photons and also serve as pump-rejection filters. We demonstrate an insertion loss of 2.37 ± 1.03 dB (4.46 ± 1.32 dB) at the visible (telecom) wavelength between the PPKTP waveguides and PIC edge couplers, and an on-chip pump suppression of 92.5 ± 2.5 dB. This platform will enable remote quantum nodes to securely communicate over telecom fiber-optic networks.

https://doi.org/10.1364/OPTICAQ.546774

1. INTRODUCTION

Quantum communication refers to the use of quantum properties of matter to encode, store, and transmit information. This emerging field promises to unlock a wide range of technological advancements, such as completely secure encryption, super-dense encoding, quantum teleportation, and metrology and sensing capabilities exceeding classical limits [1]. While many different qubit modalities are being explored for quantum computing [2–7], photons are widely regarded as the ideal "flying qubits" for long-distance quantum communication. Photonic qubits offer several advantages: they are fast, strongly couple with existing qubits while weakly coupling with the environment, and offer multiple degrees of freedom for encoding (polarization, path, orbital angular momentum, time-bin) [8]. Additionally, there already exists a vast fiber-optic infrastructure for transmitting them globally.

Many quantum networking schemes have been demonstrated using photon-pair sources based on spontaneous nonlinear processes [9–11]. These sources can generate single-photon states through heralding or use the entanglement between photon pairs as a resource [12]. Typically, long distance quantum networks are constructed with photon pairs in the telecom bandwidths to minimize transmission losses [13,14]. However, the efficient detection of telecom single photons requires superconducting nanowire single-photon detectors (SNSPDs) that are bulky and expensive [15]. This makes it difficult to develop deployable communication nodes. While there is active research focused on developing telecom-compatible, room-temperature single-photon avalanche diodes (SPADs) [16,17], their performance is yet to match that of their visible-band counterparts. To address this problem, we have developed a highly non-degenerate visible–telecom photon pair source, illustrated in Fig. 1(a). Detection at visible wavelengths can be efficiently done using compact SPADs [18], which have also been integrated on silicon photonic chips [19,20]. This eliminates the need for SNSPDs to herald, and will enable remote and deployable nodes to communicate securely with a central server as depicted in Fig. 1(b).

Furthermore, existing qubit modalities, such as trapped ions, neutral atoms, quantum dots, color centers, rare-earth-ion-doped crystals etc., are primarily interfaced with visible and near-infrared (NIR) wavelengths only [21], as shown in Fig. 1(c). A visible–telecom pair source can bridge this gap through teleportation [22], where the interaction between the node and

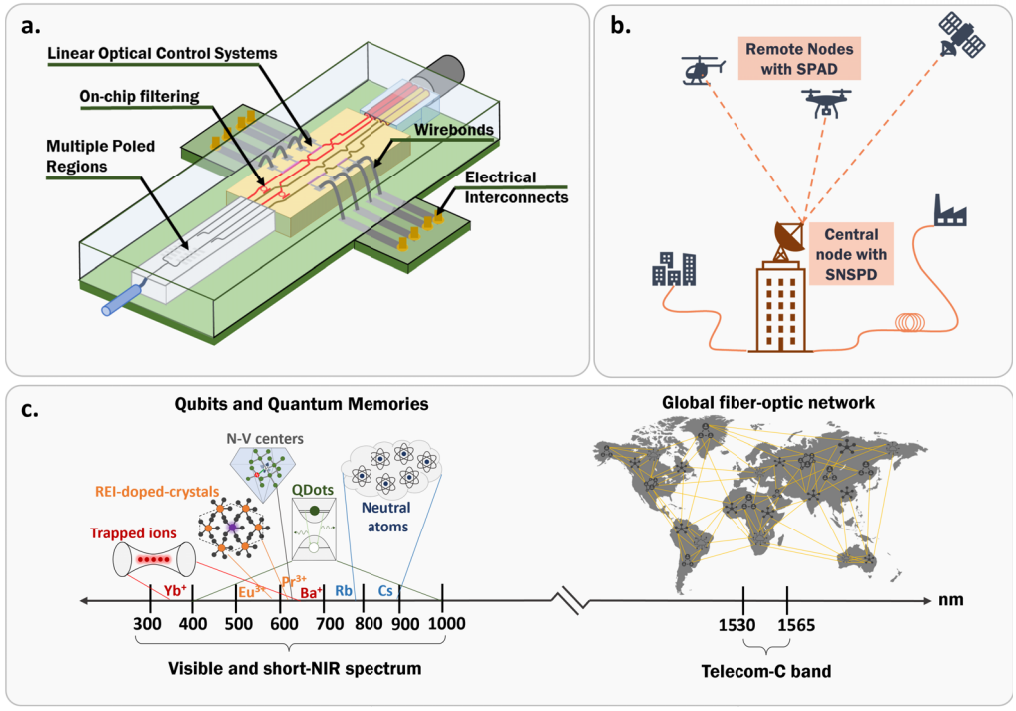

Fig. 1. Scope. (a) A representative, fully packaged version of this platform incorporating multiple poled waveguides and on-chip filters for a plug-and-play source of visible–telecom entangled photon pairs. (b) Using a visible–telecom photon pair source enables the generation of telecom single photons heralded by the visible photons. Visible wavelengths can be efficiently detected using compact single-photon avalanche diodes, while telecom wavelengths are ideal for low-loss transmission across long distances in optical fibers. Our visible–telecom pair source would allow chip-scale, field-deployable quantum nodes to securely communicate with a central server using single photons at telecom wavelengths over existing optical fibers. (c) Our visible–telecom photon pair source also paves the way for an heterogeneous quantum network by bridging the gap between various visibly accessed quantum nodes and existing telecommunication infrastructure.

the visible photon teleport the quantum state onto the telecom photon. Quantum frequency conversion (QFC) is another approach employed to downconvert a visible photon from a quantum node to the telecom band for communication over optical fibers [23–25]. This is achieved through difference frequency generation (DFG) and is limited by the noise arising out of parasitic processes such as Raman scattering and availability of suitable laser sources [26].

In both cases, the strong classical pump fields required for the nonlinear processes are >100 dB than the generated nonclassical fields and must be strongly filtered out. This is typically done using off-chip, thin-film interference filters which cause a significant loss of the photon pairs as well. On-chip filters with 100 dB of extinction have been demonstrated using cascaded ring resonators [27] and interferometers [28]. However, these suffer from high insertion losses (2–4.8 dB), and the need for careful electrical or thermal tuning of all the cascaded components to be centered on the same wavelengths. Passive filters using long Bragg gratings and tapered waveguides have been shown to be considerably broadband, offering 65–70 dB of extinction, but these are highly sensitive to fabrication variations [29–31]. Recently, it was shown that for wavelengths below 1 μm, the material absorption of silicon itself can act as a rejection filter, with over 230 dB/mm of extinction at 780 nm and less than 1 dB of insertion loss on a silicon carbide waveguide clad with a 40-nm-thick silicon layer [32]. We take a similar approach here and show that the silicon waveguides in our source can provide the necessary pump extinction as commercial off-the-shelf filters without their extra insertion losses.

2. PPKTP–PIC HYBRID PLATFORM

Nonlinear crystals make excellent photon-pair sources and have been used for several decades [33]. They operate under ambient conditions, are easy to fabricate, and straightforward to handle. These crystals use spontaneous parametric downconversion (SPDC), a $\chi^{(2)}$ nonlinear optical process, to generate photon pairs with high brightness. By employing periodic poling, the phase-matching conditions can be engineered to produce photon pairs with many different wavelength possibilities and spectral bandwidths [34]. Additionally, waveguides can be integrated into these crystals through ion-exchange [35] or direct laser writing [36]. While these waveguides greatly enhance the nonlinearity [37], they do not possess sufficient index-contrast to provide the necessary confinement for any sophisticated operations. As a result, while the source itself is compact, additional optical systems are required to manipulate and process the generated photon pairs [38]. This limits scalability, requires careful and frequent alignment, and incurs losses at each optical interface. Teleportation of the quantum state of a node to a telecom photon using PPKTP and lithium niobate (PPLN) crystals has been demonstrated previously in free-space, bench-top experiments [39–41].

However, photonic integrated circuits (PICs) offer a phase-stable and compact platform for the low-loss routing and manipulation of photons across the spectrum, as required by emerging quantum systems [42]. One of the key advantages of PICs is their compatibility with the mature complementary metal–oxide–semiconductor (CMOS) fabrication process,

which makes them both cost-effective and scalable. However, CMOS-compatible materials such as silicon, silicon nitride, and silicon dioxide are centrosymmetric, meaning they lack second-order nonlinearity. As a result, photon-pair generation in these materials relies on $\chi^{(3)}$ third-order nonlinear processes such as spontaneous four-wave mixing (SFWM), which is inherently weaker than a $\chi^{(2)}$ process. Integrated visible–telecom sources have been shown using SFWM in silicon nitride ring resonators [43] and photonic crystal fibers [44], and using five-wave mixing in aluminum nitride ring resonators [45]. These higher-order, on-chip approaches require rigorous dispersion engineering of the waveguides to phase-match across the wide spectral separation and are highly sensitive to fabrication variations.

Therefore, there is clear merit in integrating a nonlinear crystal with a PIC to leverage the complementary strengths of both platforms. Thin-film lithium niobate (TFLN)-on-insulator is one such solution aimed at developing photonic integrated circuits using highly nonlinear lithium niobate waveguides rather than silicon or silicon nitride [46]. However, challenges in wafer-scale fabrication and material challenges present significant difficulties with this approach. TFLN is not compatible with CMOS foundries due to material contamination issues caused by lithium diffusion. Additionally, LN is notoriously difficult to etch and low-roughness waveguides required for low-loss routing are not yet broadly available. TFLN could be bonded to other materials and thus can be bonded to a full silicon wafer as the final step at the back end of a standard CMOS process. Additionally, TFLN is also highly susceptible to photorefractive damage at visible wavelengths, further limiting its functionality [47].

In this work, we take a packaging-oriented approach to combine a nonlinear crystal with a PIC through direct edge coupling, as shown in Fig. 1(a). Given that fiber-coupled nonlinear waveguide sources are commercially available, and fiber-coupling is a standard procedure to couple photons on and off PICs, we aim to demonstrate the feasibility of directly coupling nonlinear waveguides to edge couplers on a PIC without any intermediate components. Such a system can be fully packaged to offer a highly customizable, stable and miniaturized platform for a wide range of quantum optical experiments. To our knowledge, such a coupled system has never been demonstrated before. We show that such a system can address our needs for highly non-degenerate visible–telecom pair generation without the caveat of excess loss of signal from pump-rejecting filters.

We use established methods of Rb-ion diffusion and periodic poling to generate visible–telecom photon pairs within PPKTP waveguides [35] at AdvR Inc. The waveguides have a nominal width of 3 μm, at a depth of 12 μm. They were uniformly poled at a period of 5.8 μm over a length of 7.5 mm for the type-0 SPDC generation of vertically polarized signal–idler photon pairs at 656 nm and 1536 nm, respectively, from a 460-nm pump. The waveguides are expected to have a maximum pair generation rate of 80 MHz/mW based on theoretical estimates for an ideal poling structure. Traditionally, these pairs are coupled into a free-space dichroic mirror or a fiber-based wavelength division multiplexer (WDM) to be separated. Instead, to allow direct coupling to a PIC, we fabricate an integrated WDM based on evanescent field coupling on the PPKTP crystal itself. The gap (6 μm) and length (1000 μm) of the coupling section are chosen such that only the telecom photons couple over to an adjacent waveguide leaving the visible photons and residual pump in the original waveguide. Such a WDM has been previously made on a lithium niobate crystal [48], but as a standalone demonstration and not for the purposes of coupling to a PIC. For added stability, the input facet of the poled waveguide is polished at an angle of 8° to minimize backreflections and attached to a polarization-maintaining Costalcon PM405 single-mode fiber pigtail, as shown in Fig. 2(b). No edge couplers are employed on the PPKTP. The output waveguides of the WDM are spaced 127 μm apart to allow for direct characterization with a standard optical fiber array. Details regarding the waveguide modes and spectral properties are stated in Section 1 of Supplement 1.

The PIC was fabricated at AIM Photonics and consists of a silicon layer (nominally 220 nm thick, 500 nm wide) and two silicon nitride layers (nominally 100 nm thick, 500 nm wide), with oxide cladding on the top and bottom [49]. We use inverse tapered edge couplers on the first nitride (FN) layer for the visible circuits (125-nm-wide tip) since this layer is optimized for low loss routing at the 500–1000 nm wavelength range through high-temperature annealing [50]. We use the second nitride (SN) layer for the telecom edge couplers (250-nm-wide tip) to reduce the interaction of this larger mode with the silicon handling wafer substrate beneath the bottom cladding. The sub-wavelength vertical offset between the two nitride layers is much smaller than the mode-field diameter of the telecom photons. Consequently, we do not observe any significant impact to the optimal positioning of the fiber array unit (FAU) or PPKTP facets for simultaneous coupling to the two channels.

We guide the visible photons entirely on the FN layer without any additional processing. On the telecom channel, we introduce a 110-μm-long tapered 'mode escalator' section to transfer the photons from the SN edge coupler to the silicon waveguide layer. We then introduce a bi-layered polarization rotator to convert the transverse-magnetic (TM) polarized telecom modes to the transverse-electric (TE) polarized mode. We then use broadband directional couplers (BDCs) (from the SiEPIC component library [51]) to form a Mach–Zehnder interferometer (MZI). N-doped-silicon-based resistive heaters are used along the arms of the MZI for thermal tuning. Except the BDC, all other components were developed for this work using ANSYS Lumerical modeling [52]. Additional details are provided in Section 2 of Supplement 1.

To demonstrate the functionality of this source, we route the visible photons across the chip and use it to herald the telecom photons. The on-chip MZI is used as a thermally reconfigurable beam splitter. This allows us to directly characterize the second-order correlation function, $g^{(2)}(\tau)$, on-chip and modulate the heralded telecom single-photon states for secure encoding. We also use the silicon waveguides in the telecom channel as passive pump-rejection filters, removing the need for any external spectral filtering.

In the following sections of the paper, we estimate the efficiency of the coupling between the PPKTP waveguides and PIC edge couplers. We compare the performance of the system with and without external spectral filters on the telecom channel, and heralding with a SPAD and an SNSPD on the visible channel. We measure the second-order coherence function of the source using the on-chip MZI. Finally, we demonstrate encoding on the SPAD-heralded telecom single photons over a >38-km-long fiber-optic network.

3. SETUP AND CHARACTERIZATION

The experimental setup used in this work is shown in Fig. 2(a). We used a Photodigm PH920DBR laser diode (8-MHz

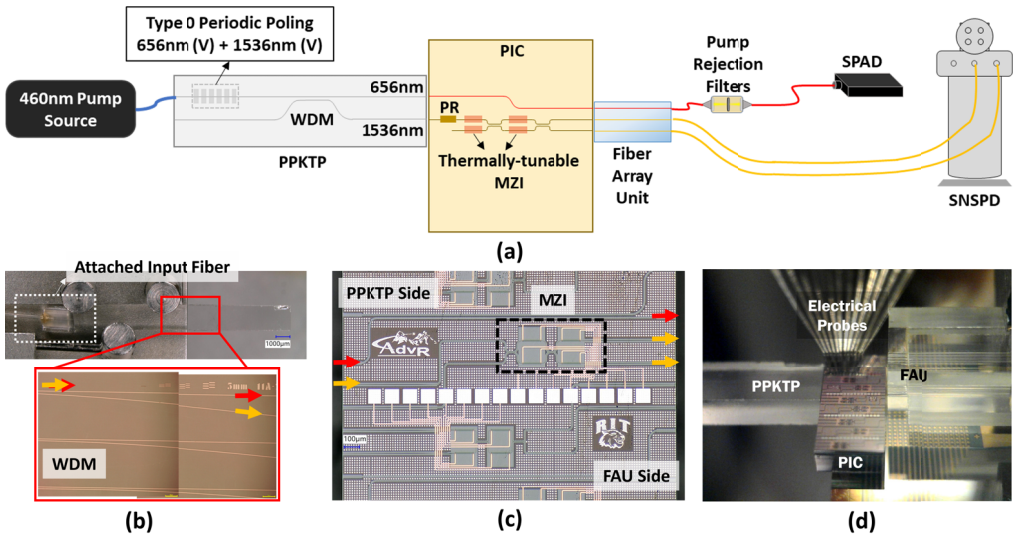

Fig. 2. Visible–telecom photon pair source on a PPKTP–PIC platform. (a) Experimental scheme: PPKTP, periodically poled potassium titanyl phosphate; WDM, wavelength division multiplexer; PIC, photonic integrated circuit; PR, polarization rotator; MZI, Mach–Zehnder interferometer; SNSPD, superconducting nanowire single-photon detector; SPAD, single-photon avalanche diode. (b) Input facet of the PPKTP is attached to a polarization-maintaining single-mode fiber. The visible–telecom pairs are generated on a periodically poled waveguide and separated using an integrated WDM shown in the inset. The red (yellow) arrows point to the visible (telecom) path. (c) Visible photon is routed directly across the chip. The telecom photon passes through an integrated MZI with thermally tunable phase-shifters on both arms. This is used to encode a message on the heralded telecom single photon. (d) Image of the testing setup showing the PPKTP, PIC, and a fiber array coupled to each other, and electrical probes for tuning the MZI.

linewidth) in conjunction with a fiber-coupled second harmonic generation (SHG) module (AdvR RSH-M0460-P85P40AL0) to generate the 460-nm continuous wave (cw) pump photons. This was directly connected to the pigtailed-input fiber (Costalcon 405PM) of the PPKTP waveguide. The PPKTP and a custom-made FAU consisting of two SM600 and two SMF28 fibers were precisely positioned using Thorlabs 6-axis flexure stages to optimally couple with the input and output edge couplers on the PIC, as shown in Fig. 2(d). A Keysight U2722A Source Measure Unit (SMU) was used to drive the on-chip heaters. Bandpass (Edmund Optics 65-110: cut-on wavelength (CWL), 656.0±2.0 nm; FWHM, 10 ± 2.0 nm; OD ≥ 4.0; blocking range, 200–1200 nm) and longpass (Edmund Optics 62-976: CWL, 500 nm; transmission WL, 508–1650 nm; OD ≥ 4.0) thin-film interference filters were used for suppressing background pump noise in the visible channel. The visible photons were then detected using either a SPAD (Perkin Elmer SPCM-EDU-CD3375H: 70% efficiency; <1000 /s dark counts; 35-ns recovery time) or an SNSPD (idQuantique id281: 76% efficiency; <5 /s dark counts; 49-ps jitter; 35-ns recovery time) based on the measurement. The telecom photons can either be filtered first using filters (Edmund Optics 85-891 Bandpass Filter: CWL, 1550 nm; FWHM, 50 nm; OD ≥ 4.0; blocking range, 200–1800 nm + Edmund Optics 62-976 Longpass filter: CWL, 500 nm; transmission WL, 508–1650 nm; OD ≥ 4.0) or directly detected with SNSPDs (idQuantique id21: 85% efficiency; <50 /s dark counts; 31-ps jitter; 86-ns recovery time). A Swabian Time Tagger Ultra (8-ps RMS jitter) was used for photon-counting and computing time-correlation statistics.

To estimate the coupling efficiency between the PPKTP and the PIC, we first characterized the components on each of them independently to determine all additional sources of loss. These steps are detailed in Sections 1(B) and 2 of Supplement 1. We list the measured values that will be relevant for estimating the coupling efficiency between PPKTP–PIC waveguides in Table 1.

Table 1. Measured Values for Estimating the Coupling Efficiency between PPKTP–PIC Waveguides[a]

Device	Measured loss (dB)
PPKTP	
Pigtailed fiber to input waveguide	3.98 ± 0.22
Visible waveguide to SM600 fiber	3.17 ± 0.22
Telecom waveguide to SMF28 fiber	3.83 ± 0.22
WDM crossover transmission	4.01 ± 0.54
PIC Visible Circuit	
Edge coupler to SM600 fiber (TM)	4.93 ± 0.21
Total propagation loss (TM)	0.54 ± 0.08
PIC Telecom Circuit	
Edge coupler to SMF28 (TE)	2.50 ± 0.21
Edge coupler to SMF28 (TM)	3.83 ± 0.21
Polarization Rotator (TM)	1.68 ± 0.42
MZI (TE)	0.50 ± 0.11
Channel losses	
Visible path	2.15 ± 0.11
Telecom path	1.33 ± 0.11

[a]All "visible" measurements were made at the signal wavelength of 656 nm and "telecom" measurements at idler wavelength of 1536 nm. The channel losses arise predominantly from the pump-rejection filters.

We also observed fluorescence close to the signal wavelength (656 nm) from the SiN waveguides on the PIC [53] (3.64 ± 0.16 MHz/μW-in-waveguide) and the optical fibers (0.09 ± 0.01 MHz/μW-in-fiber) used in the setup. This was measured by directly coupling the pump into the system and performing a power sweep. This was later subtracted from the detected singles count rates from the visible channel. Future versions of this experiment will be performed using a low-loss, low-fluorescence

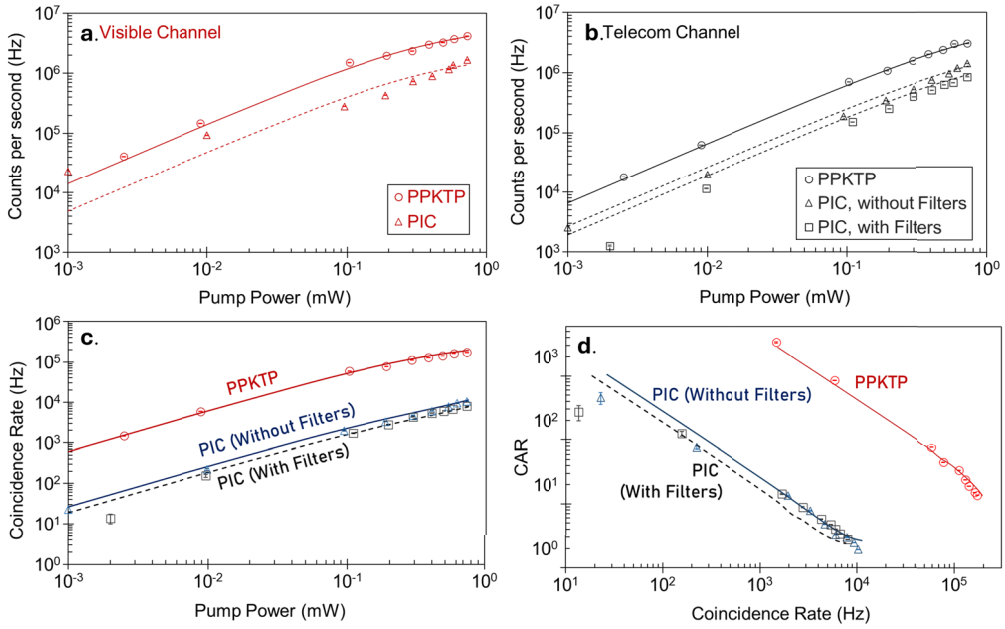

Fig. 3. Plots labeled "PPKTP" represent data collected by directly coupling a FAU to the output waveguides of the PPKTP. Those labeled "PIC" represent measurements from the hybrid PPKTP–PIC–FAU coupled system, with data taken both with and without external pump-rejection filters on the telecom channels. All data points were collected over a 10-s acquisition period. (a) Single count rates of visible photons, with the background fluorescence subtracted. (b) Single count rates of telecom photons. (c) Coincidence rates, with the background subtracted, over a 1-ns coincidence window. (d) Coincidences-to-accidentals ratio (CAR) as a function of coincidence rate. Error bars denote Poisson noise.

SiN waveguide layer [54]. Additional details are provided in Section 2(E) of Supplement 1.

4. RESULTS AND DISCUSSION

4.1. PPKTP–PIC Coupling

We first measured the signal/idler count rates, coincidence rates and coincidence-to-accidentals ratio (CAR) directly out of the PPKTP waveguides by fiber coupling to its output facet. These results are shown in the plots labeled "PPKTP" in Fig. 3. Both visible and telecom photons were filtered using pump-rejection filters and detected with SNSPDs. Measurements were taken across a range of pump powers from 1 μW to 750 μW. We use a 100-ps bin width for data acquisition and a 1-ns coincidence window to calculate the total coincidental (C) and accidental (A) counts. The CAR is then defined as (C-A)/A. Each datapoint was obtained over a 10-second acquisition. We use Poisson noise for all the detected count rates and standard error propagation for inferred values such as CAR and $g^2(\tau)$.

Next, we coupled the PPKTP, PIC, and FAU together, as shown in Fig. 2(b), and thermally tuned the phase shifters to balance the MZI, ensuring all telecom photons exited through the same port. We performed identical measurements, with and without filters on the telecom channel. These results are shown in the plots labeled "PIC" in Fig. 3.

We observed that our detected single counts saturate at rates >6 MHz in the visible channel and >4 MHz in the telecom channel. The recovery times for the visible and telecom SNSPDs imply respective saturation rates of 28.6 MHz and 11.6 MHz. We attribute the premature saturation in our counts to a combined effect of the timing electronics and a degradation of the epoxy used for the fiber-attach at the input facet of the PPKTP at higher pump powers as the crystal heats up. This reduces the amount of pump power effectively coupling into the poled waveguide diminishing pair generation. This will be rectified in future iterations using materials with better thermal stability.

To account for the saturation, we fit these data to a saturable absorber curve given by

$$C(P) = \frac{mP}{1 + P/P_{sat}}, \tag{1}$$

where $C(P)$ denotes the detected counts at a pump output power of P (not corrected for the insertion loss at the PPKTP input facet, since we consider that to be part of our system). Here, "m" corresponds to the unsaturated count rate and "P_{sat}" is the pump power at which the counts saturate.

The extracted count rates and coincidence rates from the fits are stated in Table 2. Comparing the count rates from the "PPKTP–FAU" and "PPKTP–PIC–FAU (with filters)" rows, we record that the visible and telecom photons encounter a loss of 4.67 ± 0.52 dB and 5.31 ± 0.36 dB, respectively, when coupled with the PIC.

It is important to note that the loss stated here is accumulated across the entire PIC, including all on-chip components. A comparable free-space or fiber-based setup using standard off-the-shelf components will likely incur losses of a similar or greater magnitude. From these total loss values, isolating the coupling loss at the PPKTP–PIC facet is a simple case of subtracting all other known losses in the two systems. The pump insertion loss at the PPKTP input, the WDM loss, and all channel losses are common to the two measurements. Therefore, the additional loss stated comes only from the difference between the PPKTP–FAU coupling and the sum of all PIC-related losses i.e., PPKTP–PIC coupling loss + on-PIC losses + PIC–FAU

Table 2. Unsaturated Count Rates and Coincidence Rates Estimated from Saturable Absorber Fits to the Data[a]

	Visible count rate (MHz/mW)	Telecom count rate (Mhz/mW)	Coincidence rate (kHz/mW)	Peak CAR
PPKTP–FAU	14.34 ± 1.47	6.53 ± 0.54	792.24 ± 210.01	1686 ± 44
PPKTP–PIC–FAU (with filters)	4.89 ± 0.30	1.92 ± 0.03	18.61 ± 0.38	135 ± 37
PPKTP–PIC–FAU (without filters)	4.89 ± 0.30	2.65 ± 0.11	26.49 ± 2.67	227 ± 48

[a]Uncertainties denote standard error of the fit parameters. Peak CAR reported was measured at the lowest pump power of 1 μW.

coupling loss (a step-by-step calculation is provided in Section 3 of Supplement 1). With the previously measured values from Table 1, we estimate the PPKTP–PIC coupling loss to be 2.37 ± 1.03 dB at 656 nm and 4.46 ± 1.32 dB at 1536 nm. The telecom coupling can be further improved using edge couplers specifically designed for coupling to large mode sizes [55].

Based on these values, the detected count rates, and known system losses, we can infer the intrinsic pair generation rate in the poled PPKTP waveguide to be 67.06 ± 7.24 MHz/mW, which is close to the modeled theoretical maximum of 80 MHz/mW. However, a straightforward estimate of coincidence rate based only on the pair generation rate, spurious fluorescence, channel losses, and detector efficiencies is nearly eight times larger than the detected coincidence rate. A more detailed analysis is required to systematically model the probability of coincidences given the pair generation rates and losses for all of the components in the experimental setup. Specifically, the effect of the spurious fluorescence and the large mismatch between signal and idler losses on the detected coincidence rates merits further investigation.

4.2. Pump-Filtering by Silicon Waveguides

A novel advantage of this hybrid coupling is that the pump wavelength falls within the absorption band of silicon and can be filtered by the circuit itself. To demonstrate this, we compare the detected telecom count rates, coincidence rates, and CAR with and without off-chip filters. These filters are rated to provide up to 80 dB of pump suppression but come with an insertion loss of 1.33 ± 0.11 dB.

Comparing the telecom count rates with and without filters in Table 2, we observe a gain of 1.40 ± 0.75 dB. This is in agreement with the insertion loss of the off-chip filters, within measurement uncertainty. We also record that removing these filters caused the coincidence rate to increase by a factor of 1.42 ± 0.12, with improved CAR values, as depicted in Fig. 3(d) and Table 2. Further characterization of the silicon circuit by direct coupling with the 460-nm pump laser showed a total extinction of 92.5 ± 2.5 dB. This implies that the silicon waveguides can provide better pump suppression than off-chip filters, while improving coincidence rates since they remove the additional insertion losses associated with such filters. This is particularly significant in the low-microwatt pump regime where the losses at the filter become increasingly detrimental to the CAR.

4.3. On-Chip Second-Order Correlation Measurement

Next, we computed the heralded second-order correlation function, $g^{(2)}(\tau)$, of the source following the approach in [12], given by

$$g^{(2)}(\tau) = \frac{N_{si_1i_2}(\tau)N_s(t)}{N_{si_1}(t)N_{si_2}(\tau)}, \tag{2}$$

where s corresponds to the visible signal beam and i_1, i_2 are the telecom idler split into two beams of equal intensities. Here, $N_{si_1i_2}$ is the total number of three-fold coincidences between all three beams. Additionally, N_{si_1}, N_{si_2} are the two-fold coincidences between the signal and each idler beam taken separately, and N_s is the total number of signal counts. By convention, we prepare the measurement such that s and i_1 arrive simultaneously at their detectors at time t, and define τ as the delay between t and detections of i_2. We compared two approaches: first, using a Thorlabs BXC15 50–50 beam splitter; and second, by coupling to the PIC and tuning the on-chip MZI to achieve a 50–50 splitting ratio. The measurement was run for a total duration of 5 hours in both cases. The results are shown in Fig. 4.

Data collected by directly out of the PPKTP (at 200-μW pump power, 770.14-kHz coincidences, and 21.81 CAR) yielded a $g^{(2)}(0) = 0.069 \pm 0.001$, while coupling to the PIC and using the on-chip MZI (at 70-μW pump power, 1.53-kHz coincidences, and 20 CAR) gives a $g^{(2)}(0) = 0.141 \pm 0.009$. The slight increase in $g^{(2)}(0)$ and the noise level in the dataset can be attributed to the difference in coupling efficiencies between the visible and telecom photons at the PPKTP/PIC interface and the autofluorescence from the silicon nitride waveguides. When there are more heralding visible photons than the corresponding heralded telecom photons, the probability of detecting accidental triple coincidences increases, raising the $g^{(2)}(0)$ value. To address this, we had attenuated the pump power in the second case to match the CAR value of the first case. However, this led to a reduction in all detected count rates, necessitating a longer experiment runtime. This proved challenging due to minor drifts present in the positioning instruments and random ambient disturbances, making it difficult to maintain optimal coupling at the two interfaces (PPKTP/PIC and PIC/FAU) simultaneously over time scales exceeding 8 hours. In the future, this will be addressed by fully packaging the system using a fiber-attach [56] or a photonic wire bonding process [57]. We also note that the characteristic antibunching dip appears asymmetric in Fig. 4. This is attributed to random backreflections at the PPKTP/FAU and PPKTP/PIC coupling interfaces as it occurred only close to optimal coupling condition and could be extinguished by tilting or pitching of the PPKTP and the FAU with respect to the PIC. However, in that case, the system is no longer maximally coupled. A similar asymmetry was observed in independent coincidence peaks as well. Nevertheless, the peak resides within our chosen coincidence window of 1 ns and the net detected rates are unaffected.

4.4. SNSPD-Free Heralding for Secure Encoding

The primary advantage of using a visible–telecom pair source is the ability to herald a telecom photon using a compact, room-temperature SPAD rather than a bulky and expensive SNSPD. This enables the deployment of remote nodes for secure

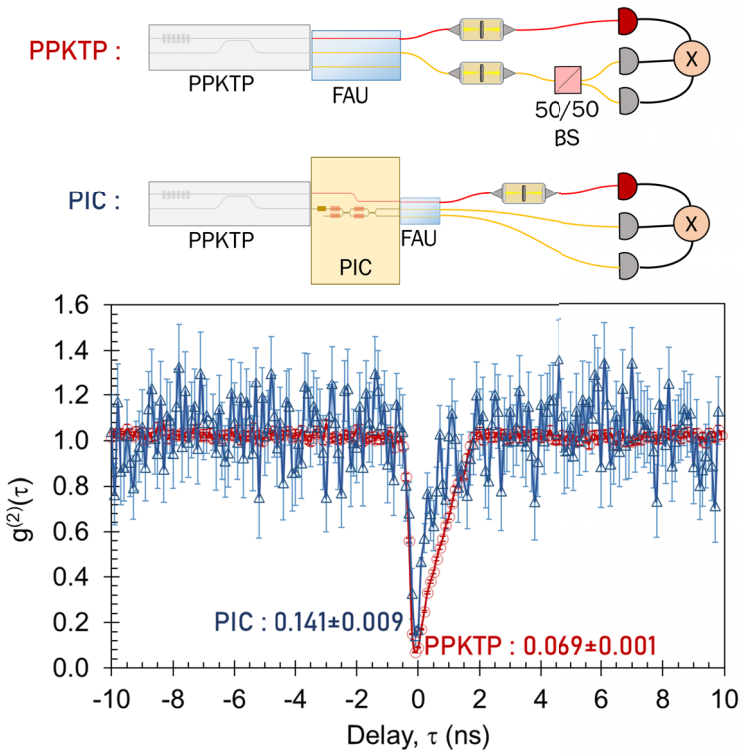

Fig. 4. Heralded $g^{(2)}(\tau)$ measurements were made by splitting the telecom channel using a Thorlabs fiber-coupled 50–50 beam splitter and the on-chip MZI. Data were collected over 5 hours for both experiments, with the pump power adjusted to maintain a consistent CAR. Error bars were calculated based on propagation of Poisson noise. The characteristic antibunch dip appears asymmetric due to random backreflections occurring at the PPKTP/FAU and PPKTP/PIC coupling interfaces. This asymmetry was observed in all independent coincidence measurements as well.

communication via messages encoded on telecom single photons through a central server. To demonstrate this, we used the tunable on-chip MZI to modulate the heralded telecom single photons. We perform the coincidence measurements at the maximum power of 750μW, with a 1-ns coincidence window and 10 s of integration time at each datapoint, for a total duration of 30 minutes per dataset.

We first used a SNSPD to detect the visible heralding photons as a reference and then switched to a SPAD. Using the SNSPD, we detected a peak coincidence rate of 11.41 ± 0.11 kHz. When switching to the SPAD, the coincidence rate dropped to 9.58 ± 0.10 kHz due to its slightly lower detection efficiency and higher dark count rates, as shown in Fig. 5(b). However, the SPAD offers significant benefits being more compact, affordable, and capable of operating at room temperature, unlike the SNSPD.

To further demonstrate the capability of this system in a real-world, long-distance quantum network, we connected the output port of the telecom photons to the Rochester Quantum Network (RoQNET). RoQNET consists of two dark optical fibers connecting the Integrated Photonics Laboratory at Rochester Institute of Technology (RIT) and the Institute of Optics at University of Rochester (UR), depicted in Fig. 5(a). For this experiment, the two fibers were connected together at UR, forming a 38-km-long loop with a total loss of 23.21 ± 0.02 dB at 1536 nm. The high loss is attributed to the numerous fiber connectors required along the network. We repeated the experiment on three different days and one trial at night to account for any environmental effects. We extended the coincidence window to 10 ns and the integration time to 60 s to compensate for the reduced counts and dispersion in the fibers. The number of data points collected was reduced to keep the total measurement time under 30 minutes, same as the previous in-lab measurements, to ensure that the system stayed optimally coupled throughout. We observed that the coincidence rates are highly diminished (peak rate of 29.02 ± 5.31 Hz) but still detectable despite the large loss and phase drifts along the channel, as shown in Fig. 5(c). Additional detail regarding the loss stability of the fiber and ambient weather conditions during measurement are provided in Section 4 of Supplement 1.

5. CONCLUSION AND OUTLOOK

We have demonstrated here that generating highly non-degenerate photon pairs in periodically poled nonlinear waveguides and directly coupling them with photonic integrated circuits serves as a promising hybrid platform for quantum photonics. This approach offers high phase stability with a much smaller device footprint compared with traditional free-space or fiber-based setups. By adjusting the poling period of the nonlinear crystal and selecting an appropriate material stack on the PIC, this platform can be tailored for a wide range of wavelengths. In this study, we coupled visible 656-nm photons and telecom 1536-nm photons from a PPKTP crystal to a PIC containing both silicon nitride and silicon circuits. A key benefit of this platform is its ability to use the silicon waveguides for suppressing the background pump noise without the insertion losses of interference filters. The PIC can be designed with circuits for a multitude of functionalities, demonstrated here by

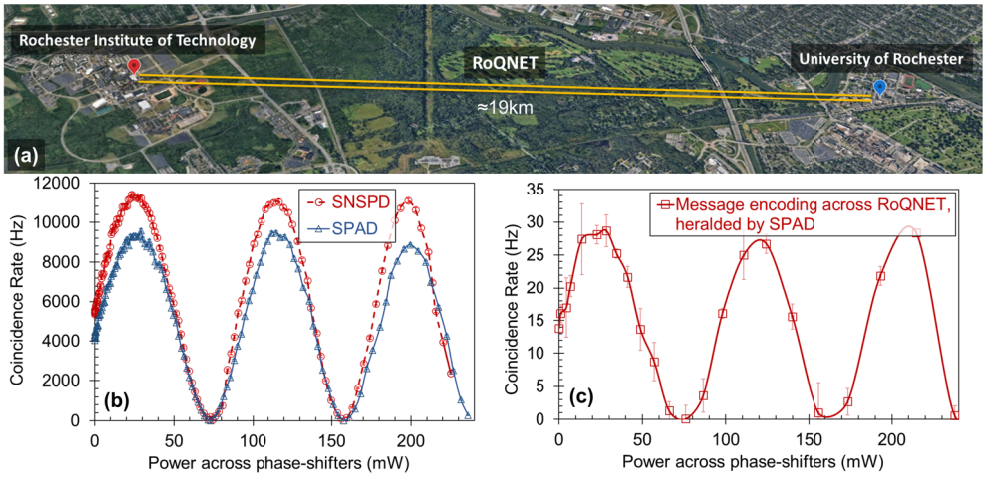

Fig. 5. (a) Two ~19-km-long dark optical fibers connecting Rochester Institute of Technology and University of Rochester form the backbone of the Rochester Quantum Network, RoQNET. (b) We compare the on-chip modulation of heralded telecom single photons using a SNSPD versus a SPAD for detecting the heralding visible photon. Each data point was collected over 10-s acquisitions with a 1-ns coincidence window. Error bars denote Poisson noise. (c) Visible photon was detected using a SPAD, and the modulated telecom single photons were transmitted through the two fiber optic cables looped together, totaling ~38 km in length, to demonstrate the performance of this hybrid visible–telecom pair source across a real-world quantum network. Error bars show the standard deviation of measurements repeated over four separate trials on different days. Due to higher losses, each data point was collected over 60-s acquisition periods with the coincidence window increased to 10 ns. Background noise was subtracted from all data points.

employing an MZI with thermo-optic phase shifters to quantify the second-order correlation function directly on-chip and modulate heralded single photons for secure message encoding. Specifically, using a visible–telecom source lets us herald the telecom single photons by detecting the visible photons with a SPAD instead of an SNSPD. This would enable quantum communication between field-deployable quantum nodes.

Comparing our PPKTP–PIC coupled system to existing integrated visible–telecom sources (Section 5 of Supplement 1), we conclude that integrating a $\chi^{(2)}$ material with a PIC produces higher pair rates than existing sources at comparable pump intensities. However, it presently suffers from uneven coupling efficiencies between the visible and telecom photons, and spurious auto-fluorescence from the waveguides which result in more visible photons than telecom photons, ultimately reducing the CAR and heralding efficiency (estimated on-chip efficiency of $5.49 \pm 1.63\%$). This can be rectified in future versions by detailed characterization of the telecom mode at the PPKTP facet and designing separate telecom input edge couplers to match it [55]. The PIC used in this work is a first, proof-of-principle demonstration and was fabricated using an un-optimized multi-project wafer (MPW) process. Future work will make use of low-loss, low-fluorescence silicon nitride waveguides [54] to address this limitation. Maintaining optimal coupling over long time scales (>8 hours) is also a major limitation at this stage. Packaging techniques to permanently attach the three components and create a robust fieldable system are currently under investigation for future experiments.

The applicability of this platform is highly versatile based on the choice of the nonlinear waveguides and the circuitry on the PIC. We are further investigating materials such as alumina and aluminum nitride that will allow us to operate over a wider spectral range, finely engineer the effective index for better mode-matching with PPKTP and optical fibers, and employ more efficient active components on-chip. Efforts to incorporate multiple poled regions on the PPTKP and PICs with highly efficient MZIs with thermal undercuts [58] on both the visible and telecom channels are also currently underway. This PIC will allow us to path-entangle the generated pairs from independent poled waveguides and ideally produce maximally entangled Bell states for quantum teleportation. Such a system could link various visible-access quantum nodes over existing telecom-compatible fiber-optic infrastructure, advancing the field of heterogeneous quantum networking.

Funding. Air Force Research Laboratory (FA8750-20-P-1709, FA8750-21-2-0004).

Acknowledgment. Any opinions, findings, and conclusions or recommendations expressed in this material are those of the author(s) and do not necessarily reflect the views of AFRL. We thank T.Stievater (NRL) for helpful discussions.

Disclosures. The authors declare no conflicts of interest.

Data availability. Data underlying the results presented in this paper are available upon reasonable request.

Supplemental document. See Supplement 1 for supporting content.

REFERENCES

1. S. Wehner, D. Elkouss, and R. Hanson, "Quantum internet: A vision for the road ahead," Science **362**, eaam9288 (2018).
2. G.-Q. Liu and X.-Y. Pan, "Quantum information processing with nitrogen–vacancy centers in diamond," Chinese Phys. B **27**, 020304 (2018).
3. C. D. Bruzewicz, J. Chiaverini, R. McConnell, *et al.*, "Trapped-ion quantum computing: Progress and challenges," Appl. Phys. Rev. **6**, 021314 (2019).
4. S. Slussarenko and G. J. Pryde, "Photonic quantum information processing: A concise review," Applied Physics Reviews **6**, 041303 (2019).
5. K. Wintersperger, F. Dommert, T. Ehmer, *et al.*, "Neutral atom quantum computing hardware: Performance and end-user perspective," EPJ Quantum Technol. **10**, 32 (2023).

6. M. Kjaergaard, M. E. Schwartz, J. Braumüller, *et al.*, "Superconducting qubits: Current state of play," Annu. Rev. Condens. Matter Phys. **11**, 369–395 (2020).
7. T. Zhong and P. Goldner, "Emerging rare-earth doped material platforms for quantum nanophotonics," Nanophotonics **8**, 2003–2015 (2019).
8. M. Krenn, M. Malik, T. Scheidl, *et al.*, "Quantum communication with photons," in *Optics in Our Time*, Vol. 18 (Springer, 2016), pp. 455–482.
9. X.-S. Ma, T. Herbst, T. Scheidl, *et al.*, "Quantum teleportation over 143 kilometres using active feed-forward," Nature **489**, 269–273 (2012).
10. C. Spiess, S. Töpfer, S. Sharma, *et al.*, "Clock synchronization with correlated photons," Phys. Rev. Appl. **19**, 054082 (2023).
11. A. Anwar, C. Perumangatt, A. Villar, *et al.*, "Development of compact entangled photon-pair sources for satellites," Appl. Phys. Lett. **121**, 220503 (2022).
12. S. Signorini and L. Pavesi, "On-chip heralded single photon sources," AVS Quantum Science **2**, 041701 (2020).
13. D. Lancho, J. Martinez, D. Elkouss, *et al.*, "QKD in standard optical telecommunications networks," in *Quantum Communication and Quantum Networking: First International Conference, QuantumComm 2009, Naples, Italy, October 26-30, 2009, Revised Selected Papers 1* (Springer, 2010), pp. 142–149.
14. Y. Zhang, Z. Chen, S. Pirandola, *et al.*, "Long-distance continuous-variable quantum key distribution over 202.81 km of fiber," Phys. Rev. Lett. **125**, 010502 (2020).
15. J. Chang, J. Los, J. Tenorio-Pearl, *et al.*, "Detecting telecom single photons with 99.5- 2.07+ 0.5% system detection efficiency and high time resolution," APL Photonics **6**, 036114 (2021).
16. N. Na, Y.-C. Lu, Y.-H. Liu, *et al.*, "Room temperature operation of germanium–silicon single-photon avalanche diode," Nature **627**, 295–300 (2024).
17. N. Na, C.-Y. Hsu, E. Chen, *et al.*, "Room-temperature photonic quantum computing in integrated silicon photonics with germanium–silicon single-photon avalanche diodes," APL Quantum **1**, 036123 (2024).
18. F. Zappa, A. L. Lacaita, S. D. Cova, *et al.*, "Solid-state single-photon detectors," Opt. Eng. **35**, 938–945 (1996).
19. F. Acerbi, M. Bernard, B. Goll, *et al.*, "Monolithically integrated SION photonic circuit and silicon single-photon detectors for NIR-range operation," J. Lightwave Technol. **42**, 2831–2841 (2024).
20. M. Sanna, A. Baldazzi, N. Broseghini, *et al.*, "Toward a room-temperature fully-integrated photonic quantum simulator," in *2024 IEEE International Conference on Quantum Computing and Engineering (QCE)*, Vol. 1 (IEEE, 2024), pp. 736–741.
21. C. Simon, M. Afzelius, J. Appel, *et al.*, "Quantum memories: A review based on the European integrated project "qubit applications (QAP)"," Eur. Phys. J. D **58**, 1–22 (2010).
22. X.-M. Hu, Y. Guo, B.-H. Liu, *et al.*, "Progress in quantum teleportation," Nat. Rev. Phys. **5**, 339–353 (2023).
23. S. Zaske, A. Lenhard, C. A. Keßler, *et al.*, "Visible-to-telecom quantum frequency conversion of light from a single quantum emitter," Phys. Rev. Lett. **109**, 147404 (2012).
24. J. Hannegan, J. D. Siverns, and Q. Quraishi, "Entanglement between a trapped-ion qubit and a 780-nm photon via quantum frequency conversion," Phys. Rev. A **106**, 042441 (2022).
25. U. Saha, J. D. Siverns, J. Hannegan, *et al.*, "Routing single photons from a trapped ion using a photonic integrated circuit," Phys. Rev. Appl. **19**, 034001 (2023).
26. P. C. Strassmann, A. Martin, N. Gisin, *et al.*, "Spectral noise in frequency conversion from the visible to the telecommunication C-band," Opt. Express **27**, 14298–14307 (2019).
27. J. R. Ong, R. Kumar, and S. Mookherjea, "Ultra-high-contrast and tunable-bandwidth filter using cascaded high-order silicon microring filters," IEEE Photon. Technol. Lett. **25**, 1543–1546 (2013).
28. M. Piekarek, D. Bonneau, S. Miki, *et al.*, "High-extinction ratio integrated photonic filters for silicon quantum photonics," Opt. Lett. **42**, 815–818 (2017).
29. N. C. Harris, D. Grassani, A. Simbula, *et al.*, "Integrated source of spectrally filtered correlated photons for large-scale quantum photonic systems," Phys. Rev. X **4**, 041047 (2014).
30. X. Nie, N. Turk, Y. Li, *et al.*, "High extinction ratio on-chip pump-rejection filter based on cascaded grating-assisted contra-directional couplers in silicon nitride rib waveguides," Opt. Lett. **44**, 2310–2313 (2019).
31. X. Guo, C.-L. Zou, and H. X. Tang, "70 dB long-pass filter on a nanophotonic chip," Opt. Express **24**, 21167–21176 (2016).
32. J. Li and A. W. Poon, "On-chip passive pump-rejection long-pass filters for integrated SiC-based nonlinear and quantum photonic chips," Opt. Lett. **49**, 411–414 (2024).
33. A. Migdall, S. V. Polyakov, J. Fan, *et al.*, *Single-photon generation and detection: physics and applications* (Academic Press, 2013).
34. M. Houe and P. D. Townsend, "An introduction to methods of periodic poling for second-harmonic generation," J. Phys. D: Appl. Phys. **28**, 1747–1763 (1995).
35. T. Zhong, F. N. Wong, T. D. Roberts, *et al.*, "High performance photon-pair source based on a fiber-coupled periodically poled $KTiOPO_4$ waveguide," Opt. Express **17**, 12019–12030 (2009).
36. A. Rodenas and A. K. Kar, "High-contrast step-index waveguides in borate nonlinear laser crystals by 3D laser writing," Opt. Express **19**, 17820–17833 (2011).
37. M. Fiorentino, S. M. Spillane, R. G. Beausoleil, *et al.*, "Spontaneous parametric down-conversion in periodically poled KTP waveguides and bulk crystals," Opt. Express **15**, 7479–7488 (2007).
38. A. Politi, J. C. Matthews, M. G. Thompson, *et al.*, "Integrated quantum photonics," IEEE J. Sel. Top. Quantum Electron. **15**, 1673–1684 (2009).
39. F. Bussières, C. Clausen, A. Tiranov, *et al.*, "Quantum teleportation from a telecom-wavelength photon to a solid-state quantum memory," Nat. Photonics **8**, 775–778 (2014).
40. A. Seri, A. Lenhard, D. Rieländer, *et al.*, "Quantum correlations between single telecom photons and a multimode on-demand solid-state quantum memory," Phys. Rev. X **7**, 021028 (2017).
41. A. Lenhard, M. Bock, C. Becher, *et al.*, "Telecom-heralded single-photon absorption by a single atom," Phys. Rev. A **92**, 063827 (2015).
42. G. Moody, V. J. Sorger, D. J. Blumenthal, *et al.*, "2022 roadmap on integrated quantum photonics," Journal of Physics: Photonics **4**, 012501 (2022).
43. X. Lu, Q. Li, D. A. Westly, *et al.*, "Chip-integrated visible–telecom entangled photon pair source for quantum communication," Nat. Phys. **15**, 373–381 (2019).
44. A. F. Khairullin, A. Smirnova, N. M. Arslanov, *et al.*, "Visible–telecom photon pair source based on a photonic-crystal fiber under continuous-wave pumping," JETP Lett. **119**, 345–351 (2024).
45. J.-Q. Wang, Y.-H. Yang, M. Li, *et al.*, "Synthetic five-wave mixing in an integrated microcavity for visible-telecom entanglement generation," Nat. Commun. **13**, 6223 (2022).
46. D. Zhu, L. Shao, M. Yu, *et al.*, "Integrated photonics on thin-film lithium niobate," Adv. Opt. Photon. **13**, 242–352 (2021).
47. G. Chen, N. Li, J. D. Ng, *et al.*, "Advances in lithium niobate photonics: Development status and perspectives," Adv. Photon. **4**, 034003 (2022).
48. S. Krapick, H. Herrmann, V. Quiring, *et al.*, "An efficient integrated two-color source for heralded single photons," New J. Phys. **15**, 033010 (2013).
49. N. M. Fahrenkopf, C. McDonough, G. L. Leake, *et al.*, "The AIM photonics MPW: A highly accessible cutting edge technology for rapid prototyping of photonic integrated circuits," IEEE J. Sel. Top. Quantum Electron. **25**, 1–6 (2019).
50. N. F. Tyndall, M. W. Pruessner, N. M. Fahrenkopf, *et al.*, "A visible-light foundry platform from aim photonics," in *2023 Optical Fiber Communications Conference and Exhibition (OFC)* (IEEE, 2023), pp. 1–2.
51. L. Chrostowski, H. Shoman, M. Hammood, *et al.*, "Silicon photonic circuit design using rapid prototyping foundry process design kits," IEEE J. Sel. Top. Quantum Electron. **25**, 1–26 (2019).
52. "Ansys Lumerical FDTD | Simulation for Photonic Components — ansys.com," https://www.ansys.com/products/optics/fdtd. [Accessed 11-02-2025].

53. M. Blasco, S. Dacunha, C. Dominguez, *et al.*, "Silicon nitride stoichiometry tuning for visible photonic integrated components," Appl. Phys. Lett. **124**, 221104 (2024).
54. N. F. Tyndall, T. H. Stievater, D. A. Kozak, *et al.*, "A low-loss sin photonic integrated circuit foundry platform for waveguide-enhanced raman spectroscopy," in *Smart Photonic and Optoelectronic Integrated Circuits XXIII*, vol. 11690 (SPIE, 2021), pp. 40–46.
55. S. F. Preble, "Quantum integrated photonics chips and packaging," in *Quantum Information Science, Sensing, and Computation XVI* (SPIE, 2024), p. PC130280F.
56. V. S. Sundaram, J. Monteleone III, V. Fittos, *et al.*, "Multi-photon-pair production in packaged, foundry-fabricated, silicon waveguide spirals," in *Quantum Information Science, Sensing, and Computation XVI*, Vol. 13028 (SPIE, 2024), pp. 117–122.
57. V. Deenadayalan, E. Thornton, G. T. Nelson, *et al.*, "Packaged tunable single mode III-V laser hybrid integrated on a silicon photonic integrated chip using photonic wire bonding," in *2024 IEEE 74th Electronic Components and Technology Conference (ECTC)* (IEEE, 2024), pp. 1387–1391.
58. M. van Niekerk, V. Deenadalayan, A. Rizzo, *et al.*, "Wafer-scale-compatible substrate undercut for ultra-efficient SOI thermal phase shifters," in *2022 Conference on Lasers and Electro-Optics (CLEO)* (IEEE, 2022), pp. 1–2.